Journal of
Materials Chemistry B

PAPER

View Article Online
View Journal | View Issue

Cite this: *J. Mater. Chem. B*, 2025, **13**, 3161

Injectable ultrathin porous membranes harnessing shape memory polymers for retinal tissue engineering†

SeongHoon Jo,‡[a] Yu-Jin Kim,‡[a] Taek Hwang,[ab] Se Youn Jang,[ac] So-Jin Park,[ad] Seongryeol Ye,[ae] Youngmee Jung *[afg] and Jin Yoo *[af]

Received 10th October 2024,
Accepted 22nd January 2025

DOI: 10.1039/d4tb02287d

rsc.li/materials-b

Age-related macular degeneration (AMD) is a leading cause of vision loss, characterized by the progressive degeneration of retinal cells, particularly retinal pigment epithelial (RPE) cells. Conventional treatments primarily focus on slowing disease progression without providing a cure. Recent advances in tissue engineering and cell-based therapies offer promising avenues for regenerating retinal tissue and restoring vision. In this study, we developed ultrathin, nanoporous membrane scaffolds designed to mimic Bruch's membrane (BrM) for RPE cell transplantation using vapor-induced phase separation. These scaffolds, fabricated from a blend of poly(L-lactide-*co*-ε-caprolactone) (PLCL) and poly(lactic-*co*-glycolic acid) (PLGA), exhibited favorable topography, biocompatibility, and shape-memory properties. *In vitro* experiments confirmed that the nanoporous topography effectively supports the formation of RPE monolayers with intact tight junctions. Additionally, the shape-memory characteristic enables the membrane to self-expand at body temperature (37 °C), facilitating minimally invasive delivery *via* injection. ARPE-19 cell-attached nanothin membranes successfully demonstrated shape-recovery properties and were deliverable through a catheter in an *ex vivo* model. Our findings suggest that the developed scaffolds provide a promising approach for retinal tissue engineering and could significantly contribute to advanced treatments for AMD and other retinal degenerative diseases.

Introduction

The retina, a delicate tissue responsible for sensing light, is susceptible to degenerative conditions.[1] Anatomically, it can be divided into inner and outer layers. The inner layer contains neuronal cells called photoreceptors, while the outer layer consists of highly specialized pigmented cells known as retinal pigment epithelial (RPE) cells.[2–4] The RPE forms a monolayer of non-regenerative cells crucial for vision maintenance and is separated from the choriocapillaris by Bruch's membrane (BrM).[5,6] Age-related macular degeneration (AMD) is one of the most common retinal degenerative diseases, which is a progressive and multifactorial neurodegenerative disease.[7] Several protocols exist for managing AMD, including intravitreal drug administration and vitreoretinal surgery. However, these strategies aim to delay disease progression rather than provide a cure.

Therefore, to achieve a fundamental cure, cell-based therapies that can regenerate the retina are attracting attention as promising treatments for retinal diseases. While gene therapy shows potential for early-stage intervention, cell therapy and tissue engineering (TE) are more suited to treating advanced stages of the disease. Recently, TE of the human retina has garnered increasing attention with the goal of restoring retinal function and preventing vision loss. Numerous clinical trials have transplanted RPE cells derived from human embryonic stem cells (hESCs) or induced pluripotent stem cells (iPSCs).[8,9] The simplest method to deliver these cells to the retina is through direct injection of a cell suspension into the subretinal region.[10] However, without scaffolds, transplanted RPE cells

---

[a] Biomaterials Research Center, Biomedical Research Division, Korea Instituten of Sicence and Technology (KIST), Seoul 02792, Republic of Korea. E-mail: winnie97@kist.re.kr, jyoo@kist.re.kr

[b] Department of Metabiohealth, Sungkyun Convergence Institute, Sungkyunkwan University (SKKU), Suwon 16419, Republic of Korea

[c] KU-KIST Graduate School of Converging Science and Technology, Korea University, Seoul 02841, Republic of Korea

[d] School of Chemical Engineering & Materials Science, Chung-Ang University, Seoul 06974, Republic of Korea

[e] Department of Applied Bioengineering, Graduate School of Convergence Science and Technology, Seoul National University, Seoul 08826, Republic of Korea

[f] Division of Bio-Medical Science and Technology, KIST School, Korea University of Science and Technology (UST), Seoul 02792, Republic of Korea

[g] School of Electrical and Electronic Engineering, YU-KIST Institute, Yonsei University, Seoul 03722, Republic of Korea

† Electronic supplementary information (ESI) available. See DOI: https://doi.org/10.1039/d4tb02287d

‡ These authors contributed equally to this work.

often fail to adhere to BrM and tend to form aggregates rather than a normal monolayer.

Biomaterial scaffolds can enhance the delivery and integration of retinal cells or tissues, either as injectable or preformed structures, promoting cell adhesion at the sub-macular level and improving retinal tissue formation *in vitro* before transplantation.[7,11] These cell-based scaffold complexes are injected under the retina, where they replace abnormal RPE cells, restore their function, and halt disease progression.[12,13] Additionally, cells transplanted with scaffolds maintain cell-to-cell contact, unlike single cells, which help retain the epithelial-like morphology of RPE cells and facilitate monolayer epithelization. Compared to free cell suspension techniques, the presence of the extracellular matrix (ECM) allows for easier and faster adhesion and attachment to the host tissue without any pre-treatment. Notably, cell-based strategies using artificial scaffolds have shown the ability to maintain well-organized and healthy RPE cells, enhancing cell survival and mitigating the deteriorative behaviors associated with aged RPE.[14–17]

For retinal TE, the scaffold development should ideally replicate BrM in terms of its permeability and flexibility, as BrM naturally supports RPE cells.[18–20] This mimicry is essential to avoid damaging surrounding tissues. Additionally, scaffolds for TE should meet two critical requirements: biocompatibility and biodegradability.[21–23] Scaffolds made from synthetic biomaterials have been designed in a reproducible and predictable manner, with optimized mechanical strength, degradation rate, and microstructure. Consequently, synthetic biocompatible polymers, such as poly(L-lactic-*co*-glycolic) acid (PLGA) and poly(ε-caprolactone) (PCL), have been employed for biomedical applications where degradation is necessary.[24]

In this research, we designed ultrathin supporting membranes with favorable topography to replicate BrM for tissue-engineered retinal RPE transplantation. To mimic the key characteristics of BrM, such as its nanoporous structure, elasticity, and barrier function, these ultrathin membranes are designed to be free-standing, flexible and nanoporous.[25] Additionally, the developed membranes, designed for the injection-based delivery of RPE cell-attached constructs *via* a needle or catheter, possess shape-memory properties and autonomously expand at 37 °C, closely matching body temperature. To create a shape memory polymer-based membrane for retinal TE, a polymer blending method was adopted; the poly(L-lactide-*co*-caprolactone) (PLCL) and PLGA blend ratio was optimized to maximize the shape memory effect.[26] Furthermore, to induce the porous structure on the membrane for mimicking the BrM, the vapor-induced phase separation (VIPS) method was applied during a spin-coating process, resulting in ultrathin nanoporous membranes.[27–31] It was confirmed that the developed membrane exhibited high biocompatibility by providing an environment conducive to forming ARPE-19 cell (from human RPE cell line primary cultures) monolayers, which enables the development of normal tight junctions *in vitro*.[32] Additionally, the ARPE-19 cell-attached membranes could be delivered by injection through a catheter due to their shape-recovery nature at 37 °C in an *ex vivo* model (Scheme 1).

Results and discussion

Fabrication of injectable ultrathin porous membranes (IUPMs)

To impart shape-memory properties to the membrane, injectable ultrathin porous membranes (IUPMs) were synthesized by

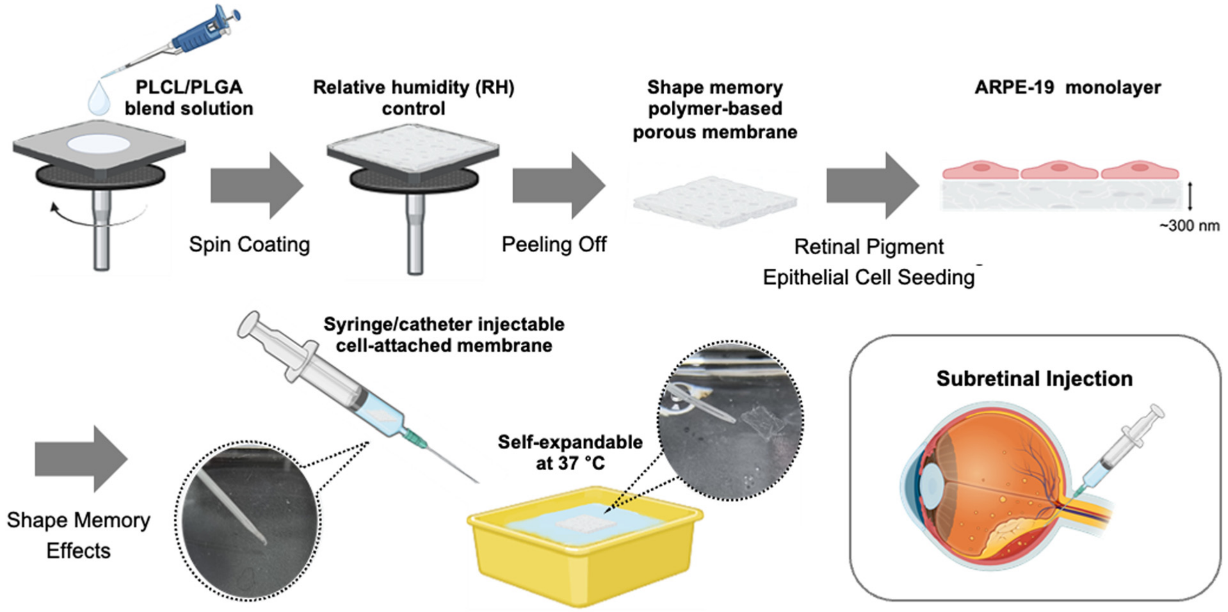

Scheme 1 Schematic illustration of the preparation and delivery process of the injectable ultrathin porous membrane (IUPM) incorporated with ARPE-19 cells, forming the APRE-19/IUPMs construct. The scheme also highlights potential applications for subretinal injection in retinal therapies. The figure was created with **https://BioRender.com**.

blending PLCL and PLGA, as previously described.[26] Both PLCL and PLGA are FDA-approved,[33,34] biocompatible materials suitable for biomedical applications.[35,36] Polymer blends are one of the classifications of shape-memory polymers.[37] The observation of two distinct T_g values in the PLCL/PLGA blend indicates a degree of micro-phase separation, which is essential for its shape-memory behavior (Fig. S1, ESI†). In this system, PLCL acts as the soft phase due to its high flexibility and elastomeric properties, characterized by a relatively low T_{g1}. This soft phase contributes to the material's plasticity and facilitates deformation and recovery. In contrast, PLGA serves as the hard phase, providing a robust physical network for structural stability. With its higher T_{g2}, PLGA forms stable physical crosslinks at low temperatures, aiding in shape fixation. This shape-memory functionality relies on physical phase separation rather than chemical crosslinking, similar to SEBS (polystyrene-poly(ethylene-*co*-butylene)-polystyrene) elastomers.[38]

The shape-memory mechanism of the PLCL/PLGA system involves two distinct phases: shape fixation and shape recovery (Scheme 2). During shape fixation, deformation occurs at elevated temperatures when the PLCL soft phase transitions into a rubbery state, enabling easy deformation. Concurrently, the PLGA hard phase forms a stable network, locking the deformed shape as the system cools. Once cooled to T_{g1} (~ 0 °C), the PLCL phase transitions into a glassy state, preserving the deformed structure. In the shape recovery process, heating the system to the transition temperature (~ 37 °C) causes the PLCL soft phase to soften and release the stored deformation. Meanwhile, the PLGA hard phase retains its stability, ensuring an effective recovery process.

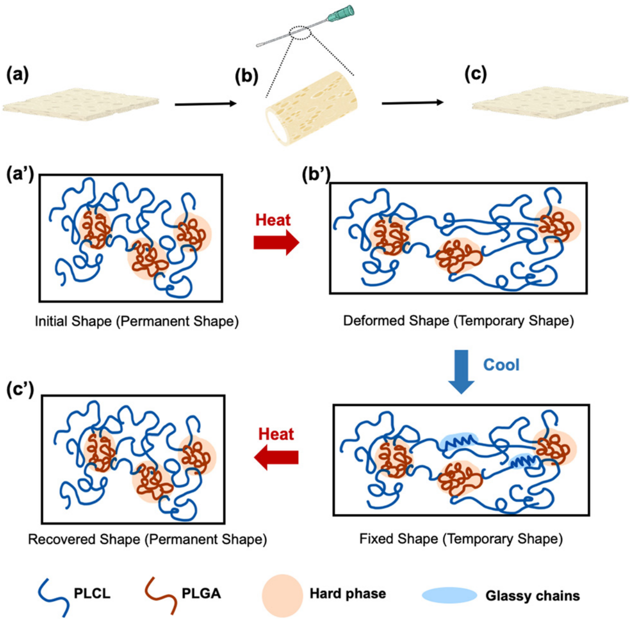

Scheme 2 Schematic illustration of the thermally induced shape-memory process in PLCL/PLGA blend systems. (a) Polymeric blend membranes in their initial shape, accompanied by (a′) a schematic representation of the polymer structures. (b) The deformed membrane, compressed and inserted into a catheter or needle, and (b′) the corresponding schematic showing the PLGA hard phase maintaining structural stability. Upon cooling, the PLCL phase transitions into a glassy state, preserving the deformed structure. (c) and (c′) During the shape recovery process, heating the system to the transition temperature softens the PLCL soft phase, releasing the stored deformation. As a result, the membrane self-expands in a warm water bath.

To mimic BrM for scaffold applications, the polymer blend membranes are needed to achieve nanoporous structures. Membranes with varying blend ratios and a consistent polymer concentration of 5% (w/v), (PLCL1/PLGA2, PLCL1/PLGA1, and PLCL2/PLGA1) were fabricated under different relative humidity (RH) conditions and analyzed using a scanning electron microscope (SEM) to assess the porous structures and pore size (Fig. 1). The VIPS method was employed during the spin-coating to fabricate nanoporous and ultrathin membranes. Since water vapor acts as a non-solvent, controlling the relative humidity helped create the nanoporous structure on membrane surfaces.[30]

The SEM images revealed distinct variations in the porous structure depending on the blend ratios. The PLCL2/PLGA1 solution failed to form porous structures at any of the RH levels (40, 60, and 80%), likely due to the hydrophobic nature of PLCL, which inhibits water vapor penetration into the polymer solution. In contrast, porous surfaces were achieved with PLCL1/PLGA1 and PLCL1/PLGA2 at higher RH levels (60% and 80%). All blend ratios at RH 40% showed surfaces without pores. It PLCL's higher hydrophobicity compared to PLGA, resulting in insufficient water vapor penetration.[27,30] As humidity increased, the pore size also increased due to the condensation and merging of water droplets on the polymer solution surface.[39]

Shape-memory properties of polymer blends

To maximize the shape-memory effect for easy injectability, we investigated the shape-memory behavior of membranes with varying blend ratios of PLCL to PLGA. Specifically, we analyzed PLCL1/PLGA1 and PLCL1/PLGA2 membranes, excluding PLCL2/PLGA1 since it could not achieve porous structures

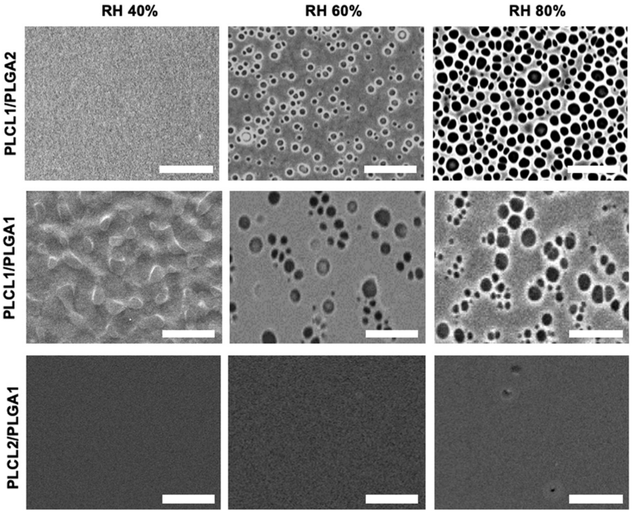

Fig. 1 Fabrication of IUPMs with different blending ratios of PLCL and PLGA. SEM images of IUPMs fabricated under different relative humidity conditions (40%, 60%, and 80%, scale bar = 10 μm).

using the VIPS technique. This section primarily focuses on the influence of blending ratios of PLCL and PLGA on shape recovery properties. To this end, we conducted physical property characterization using non-porous membranes. The shape memory behavior of the membranes was evaluated through dynamic mechanical analysis (DMA) measurements, employing a stagewise heating program in the stress control mode.

Fig. 2a presents 3D plots illustrating the thermomechanical behavior of PLCL1/PLGA1 and PLCL1/PLGA2 during different phases: unloading, fixing, cooling, and recovery, analyzed through DMA. The plots depict the relationship between temperature, stress, and the shape-recovery ratio (R_r). The shape-memory capabilities of the polymers are driven by their thermal and mechanical properties, which induce deformation and stress at specific temperatures.[40]

The transition temperature ($\sim$37 °C) lies between two T_g values and represents a critical point where interactions between the soft PLCL and hard PLGA phases occur. At this temperature, the PLCL soft phase begins to soften, while the PLGA phases remain stable, allowing the system to initiate the shape recovery process. The DMA analysis revealed that the R_r value of PLCL1/PLGA1 was 68.67%, significantly higher than the 33.86% observed for PLCL1/PLGA2. In contrast, the fixity ratio (R_f) of PLCL1/PLGA1 was 97.06%, compared to 98.36% for PLCL1/PLGA2. These results highlight the significant influence of the PLGA-to-PLCL ratio on the R_f and R_r in PLCL/PLGA blends. A higher PLGA content increases R_f due to the robust physical network formed by the hard phase, which enhances the material's ability to maintain a fixed shape. However, it reduces R_r, as the rigid PLGA phase limits flexibility and hinders the recovery process. Conversely, a higher PLCL content improves R_r due to the soft phase's low T_g and high elasticity, which facilitate deformation and recovery. However, it decreases R_f, as the more deformable PLCL phase struggles to maintain the fixed shape.

In accordance with the shape-memory behavior, the mechanical properties, including Young's modulus and tensile stress, were measured using a universal testing machine (UTM) (Fig. 2b). The stress–strain curve highlights the mechanical behavior of the PLCL1/PLGA1 and PLCL1/PLGA2 under tensile stress, demonstrating an initial elastic region followed by a plastic deformation phase. The modulus of resilience, defined as the ability of a material to absorb energy per unit volume without yielding or entering the plastic zone, provides insight

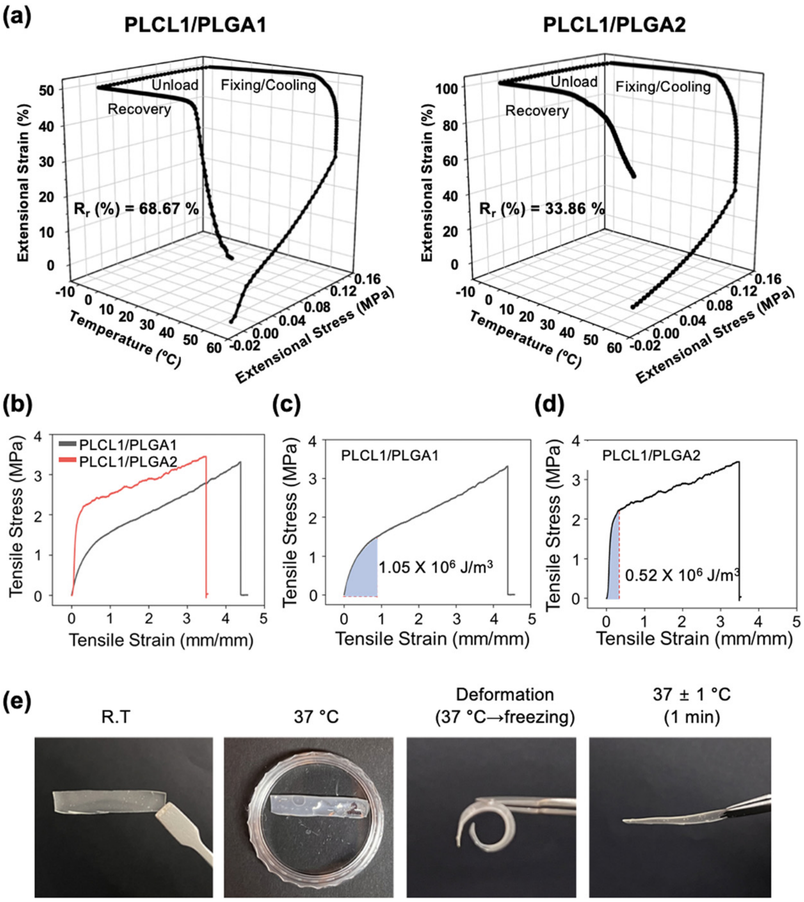

Fig. 2 (a) Shape-memory effects of the films evaluated using DMA, with the left graph showing the results for the PLCL1/PLGA1 specimen and the right graph for the PLCL1/PLGA2 specimen. (b) Tensile stress–strain curves of films measured using a UTM. Modulus of resilience calculated from the stress–strain curves for (c) PLCL1/PLGA1 and (d) PLCL1/PLGA2, with the yield point determined using a 0.2% offset. (e) Shape-memory behavior of the film with a PLCL1/PLGA1 blending ratio.

into the material's capacity to withstand deformation without experiencing permanent damage.[41]

When comparing the modulus of resilience in the stress–strain curve, the value for PLCL1/PLGA1 was 1.05×10^6 J m^{-3}, while for PLCL1/PLGA2, it was 0.52×10^6 J m^{-3} (Fig. 2c and d). Resilience is defined as the ability of a material to absorb energy during deformation and subsequently recover its original state after unloading.[42] High resilience in shape memory polymers enhances their ability to return to their original shape following deformation and fixation processes.[43] As such, the modulus of resilience is closely associated with the shape memory effect. This correlation is demonstrated by the higher modulus of resilience observed for PLCL1/PLGA1, which corresponds to a higher R_r. The greater resilience of PLCL1/PLGA1 suggests a superior capacity for elastic energy storage, leading to enhanced shape recovery performance. The stress–strain curves also suggested that PLCL1/PLGA2 has a higher Young's modulus compared to PLCL1/PLGA1 (Fig. S2, ESI†). The value for PLCL1/PLGA1 was 1.77 MPa and for PLCL1/PLGA2 was 5.35 MPa, indicating that PLCL1/PLGA2 is stiffer compared to PLCL1/PLGA1. Since PLGA has higher stiffness than PLCL,[44] the Young's modulus value of PLCL1/PLGA1, with a smaller composition ratio of PLGA, appeared to be lower than that of PLCL1/PLGA2.[45] Fig. 2e highlights the excellent shape-memory effect exhibited by the PLCL1/PLGA1 composition. Additionally, the tensile strength and Young's modulus of the porous ultrathin PLCL1/PLGA1 IUPMs were measured using a UTM (Fig. S3, ESI†). Notably, no significant differences in the physical properties were observed when compared to the non-porous membranes. Furthermore, as demonstrated in Fig. S4 (ESI†), the porous IUPMs with a PLCL1/PLGA1 composition also exhibited robust shape-memory effects.

Characterization of injectable ultrathin porous membranes (IUPMs)

SEM images, along with shape-memory behavior and mechanical properties, indicated that PLCL1/PLGA1 is well-suited for mimicking BrM and achieving optimal shape-memory effects. Since PLCL1/PLGA1 achieved a nanoporous structure through the VIPS method and demonstrated superior shape-memory behavior and resilience, it was considered the most suitable option for application to retinal tissue engineering.

The pore morphologies of the membranes with the optimized blend ratio (PLCL1/PLGA1) were characterized by atomic force microscopy (AFM), as shown in Fig. 3a. The average pore size was 520 ± 350 nm at RH 60% and 960 ± 530 nm at RH 80%. Relative humidity and mass exchange rates were adjusted to create a nanoporous structure in the membrane, using water vapor as a non-solvent. The average water contact angle of the membranes at RH 40% was 82.3 ± 2.0°, at RH 60% was 83.5 ± 1.8°, and at RH 80% was 83.5 ± 3.1°, as shown in Fig. 3b. Despite variations in the surface morphologies of the IUPMs

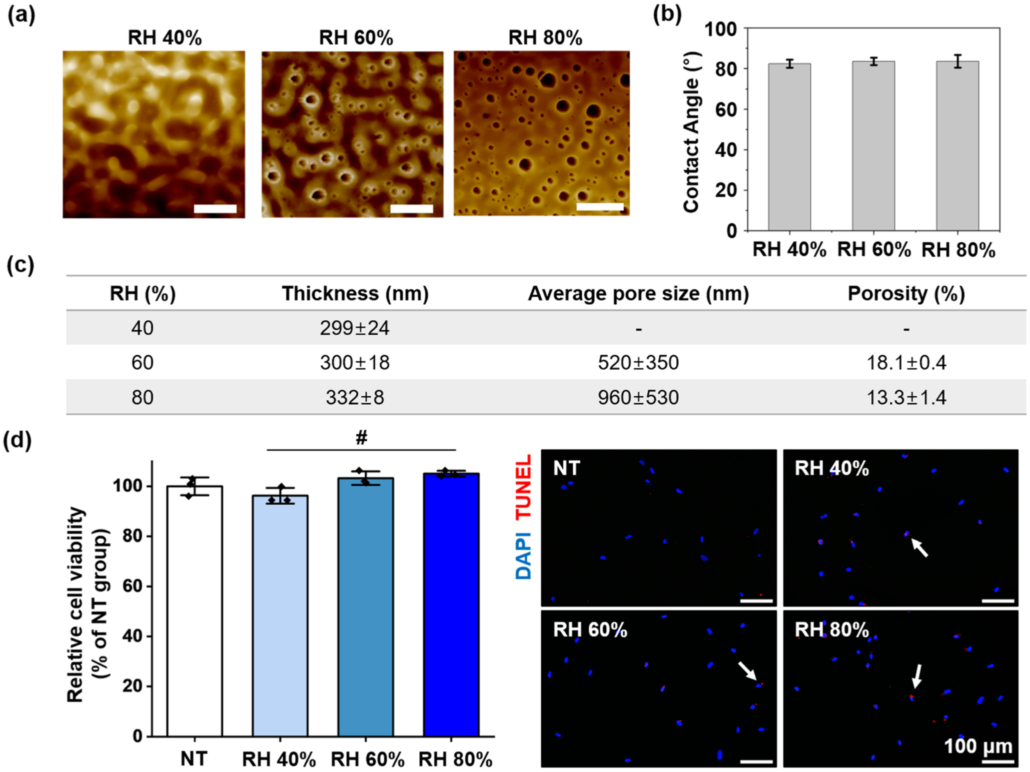

RH (%)	Thickness (nm)	Average pore size (nm)	Porosity (%)
40	299±24	-	-
60	300±18	520±350	18.1±0.4
80	332±8	960±530	13.3±1.4

Fig. 3 Characterization of pore size, thickness, hydrophilicity, and cytotoxicity of IUPMs (a) AFM images of IUPMs at different RH levels (scale bar = 5 μm). (b) Hydrophilicity of IUPMs assessed by contact angle measurements. (c) Quantification of physical properties of IUPMs at different RH levels. (d) Cytotoxicity evaluation of IUPMs using the NR assay and TUNEL staining. The intact nuclei are marked by blue DAPI staining, while apoptotic cells are indicated by red fluorescence (highlighted with white arrows). ($^{\#}p < 0.05$ compared to each other; $n = 3$).

under different RH conditions, these differences had a negligible effect on the water contact angle of the membranes.

Additionally, the spin-coating process, performed in a closed system, enabled the fabrication of nano-thin membranes while maintaining constant RH conditions.[46,47] The thickness of the membranes was consistent across different RH conditions, with values of 299 ± 24 nm, 300 ± 18 nm, and 332 ± 8 nm at RH 40%, 60%, and 80%, respectively, as shown in Fig. 3c. For retinal tissue engineering applications, implanting scaffolds thicker than the retina can pose a risk of retinal damage or detachment. The BrM itself has an approximate thickness of 2–4 μm.[6,11] In contrast, the membrane developed in this study is an ultrathin structure, measuring only ∼300 nm. This ultrathin property is particularly advantageous as it minimizes the risk of retinal damage and allows for the potential injection of multiple layers without adverse effects.

Cytotoxicity of the IUPMs was assessed using the neutral red (NR) assay (Fig. 3d). The results demonstrated that the IUPMs supported robust cell growth, with high viability observed. Quantitative analysis indicated that cells cultured on the IUPMs exhibited similar viability to those cultured on tissue culture plates (NT group), as evidenced by their ability to uptake the neutral red dye. To further evaluate the cytotoxic effects and identify apoptotic cells, TUNEL staining was performed (Fig. 3d). The TUNEL staining results revealed a low level of apoptosis in cells grown on the IUPMs, indicating that the majority of cells remained viable and did not undergo significant apoptotic cell death. The results from the NR assay and TUNEL staining collectively demonstrate that the IUPMs support healthy cell growth with minimal cytotoxicity. These findings are crucial for the potential application of IUPMs in retinal regeneration, as they highlight the ability of the IUPMs to maintain viable and functional cells. The biocompatibility of the IUPMs suggests that they can serve as a supportive scaffold for retinal cells, thereby promoting tissue repair and regeneration.

Assessment of the epithelial barrier formation

The expression of F-actin was assessed using fluorescence staining, and the results indicated that the IUPMs prepared at RH 60% exhibited F-actin expression similar to that of the NT group. This suggests that the structural integrity and cytoskeletal organization of cells in the RH 60% IUPM group were well-maintained. Additionally, ZO-1 expression, a marker for tight junctions and epithelial barrier function, was evaluated through fluorescence staining (Fig. 4a). Among the groups, the RH 60% IUPM group showed the highest ZO-1 expression, indicating superior tight junction formation and barrier integrity compared to the other groups. Notably, the expression levels of F-actin were higher in the RH 60% and RH 80% IUPM groups compared to the RH 40% IUPM group. This increase can be attributed to the enhanced surface area provided by the pores, which promotes better cell attachment.[48] Specifically, the increased expression of ZO-1 in the RH 60% IUPM group is likely due to the smaller pore size, which more closely mimics BrM and facilitates improved cell-to-cell interactions.[49,50] Consequently, the RH 60% IUPM group demonstrated the most favorable conditions for cell attachment.

To further investigate the molecular characteristics of the cells, the expression of *ZO-1*, *CLAUDIN*, *RPE65*, and *CRALBP* were compared between the NT and at RH 60% IUPM groups (Fig. 4b). The results showed that the RH 60% IUPM group had higher expression levels of *CLAUDIN* and *CRALBP* genes compared to the NT group, suggesting enhanced tight junction integrity and improved functionality of retinal pigment epithelium (RPE) cells in the RH 60% IUPM group. Conversely, the expression levels of *ZO-1* and *RPE65* were similar between the NT and RH 60% IUPM groups, indicating that the basic epithelial and retinal cell properties were maintained across both groups. These results highlight the potential of the RH 60% IUPM group for retinal regeneration applications. The ability of these cell culture membranes to support robust cytoskeletal organization, tight junction formation, and gene expression profiles indicative of functional RPE cells underscores their suitability for therapeutic use.

Catheter-injectability and self-expandability of IUPMs

Considering the potential *in vivo* applications of IUPMs as scaffolds for tissue-engineered retinal RPE transplantation, this study aimed to develop IUPMs that are catheter-injectable and self-expandable. The catheter-injectability and self-expandability of IUPMs were demonstrated, as illustrated in Fig. 5. First, the IUPM was heated to 37 °C and then deformed. After freezing for 20 minutes, the deformed IUPM was injected into a 37 °C water bath using 5 mL of water through a 16-gauge catheter attached to a 10 mL syringe under manual pressure. As shown in Fig. 5a, the IUPM was easily extruded through the catheter. Upon extrusion into the water bath, the IUPM expanded back to its original flat membrane form (Movie S1, ESI†).

The IUPMs' high flexibility and nanothin thickness enabled their placement and injection through the catheter. This flexibility offers a key advantage in cell delivery, allowing for intact subretinal transplantation of cell-attached membranes. Catheter injection provides a minimally invasive approach, potentially reducing scleral incision size and minimizing associated inflammatory response. To explore this capability, APRE-19 cells were cultured on IUPMs. Live/dead staining demonstrated that the IUPMs, along with the ARPE-19 cell monolayer, remained stable and maintained cellular viability throughout catheter injection (Fig. 5b). At all stages—room temperature, 37 °C, deformation, and recovery—APRE-19 cells exhibited high viability as shown in Fig. 5c. The majority of cells remained alive (green) on the IUPMs after deformation, freezing, recovery, and extrusion. These results confirm the feasibility of using ultrathin porous membranes for the delivery of ARPE-19 cell monolayers in tissue-engineered retinal RPE transplantation.

However, as depicted in Fig. 5d, the IUPMs did not expand and remained crumpled when submerged in water baths at 4 °C and 25 °C. This failure to recover is attributed to insufficient phase transitions or endothermic reactions required for shape recovery, driven by the movement of the soft PLCL component. These observations align with the DMA results, which indicate that the transition temperature of PLCL1/PLGA1 is approximately 36 °C. Overall, these findings strongly suggest that the

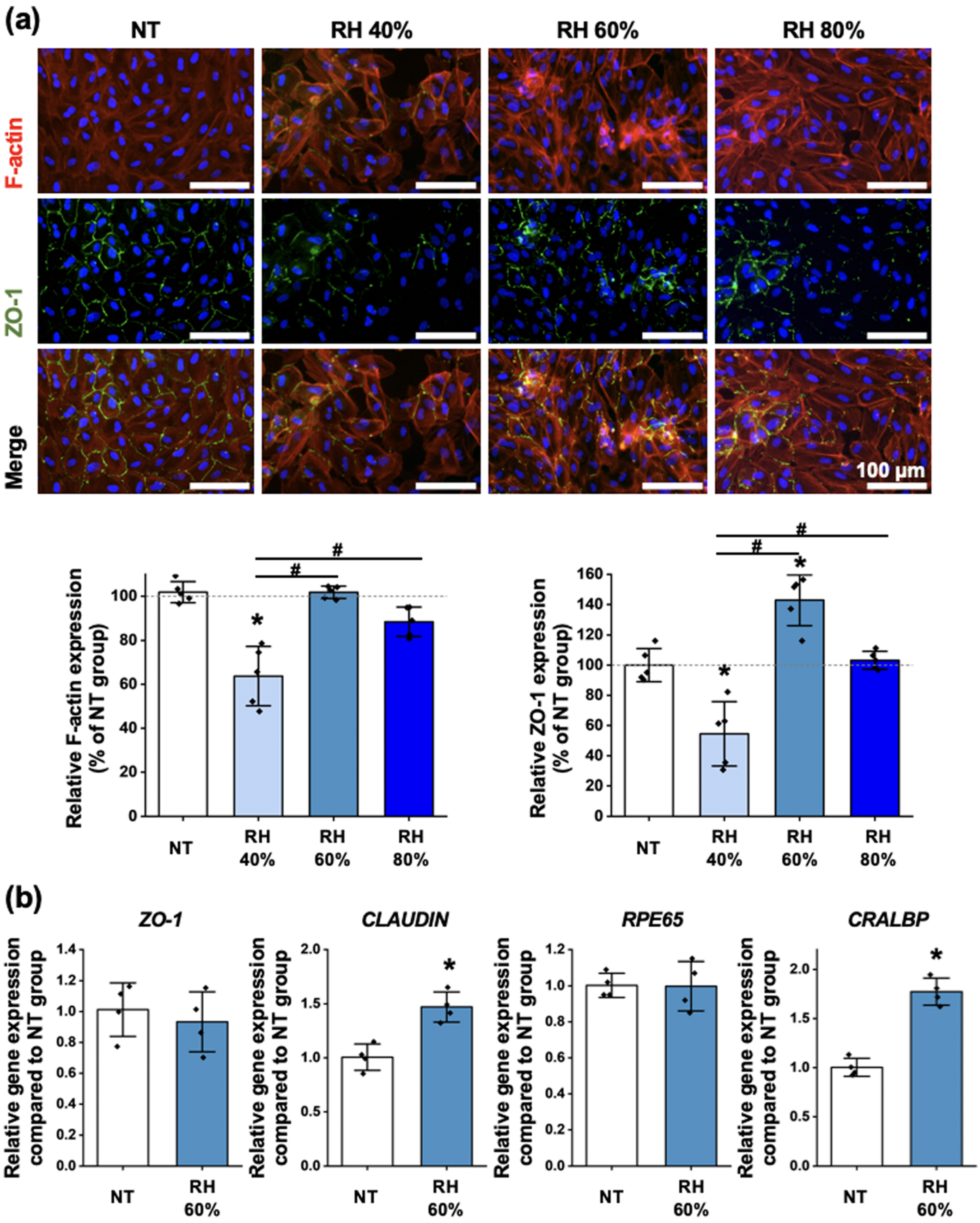

Fig. 4 Fluorescence staining and gene expression analysis of IUPMs. (a) Fluorescence staining for F-actin (red), ZO-1 (green), and DAPI (blue) in NT and IUPMs. The graph on the right depicts the quantitative analysis of protein expression based on staining intensity. Scale bar = 100 μm. (*$p < 0.05$ compared to the NT group; $^{\#}p < 0.05$ compared to each other; $n = 5$) (b) relative mRNA expression of *ZO-1*, *CLAUDIN*, *RPE65*, and *CRALBP* in the NT and RH 60% IUPM group. (*$p < 0.05$ compared to the NT group; $n = 4$).

self-expandability of the IUPMs is exclusively by the temperature-mediated shape-memory effect, rather than structural or mechanical properties or external shear forces.

Ex vivo experiments were conducted to assess the feasibility of delivering IUPMs into the subretinal space. Prior to IUPM injection, the subretinal space was partially filled with PBS to secure the implantation site (Fig. 5e).[51] The IUPM, pre-stained with rhodamine B (7 × 7 mm), was successfully injected and deployed into the subretinal space using a 16-gauge intravenous catheter. Once in place, the IUPM adhered to the target site and retained its structural integrity (Fig. 5f). The retina, situated between the retinal photoreceptors and choroid membranes, facilitated stabilization of the RPE cell adhesion membrane by allowing the prefilled PBS to be removed. Thus, the *ex vivo* results confirmed the practicality of using IUPMs for delivering RPE cell monolayers. Furthermore, the cell density on the IUPM can be adjusted to match the size of the AMD lesion, enhancing the clinical applicability of this approach. These results suggest that the high

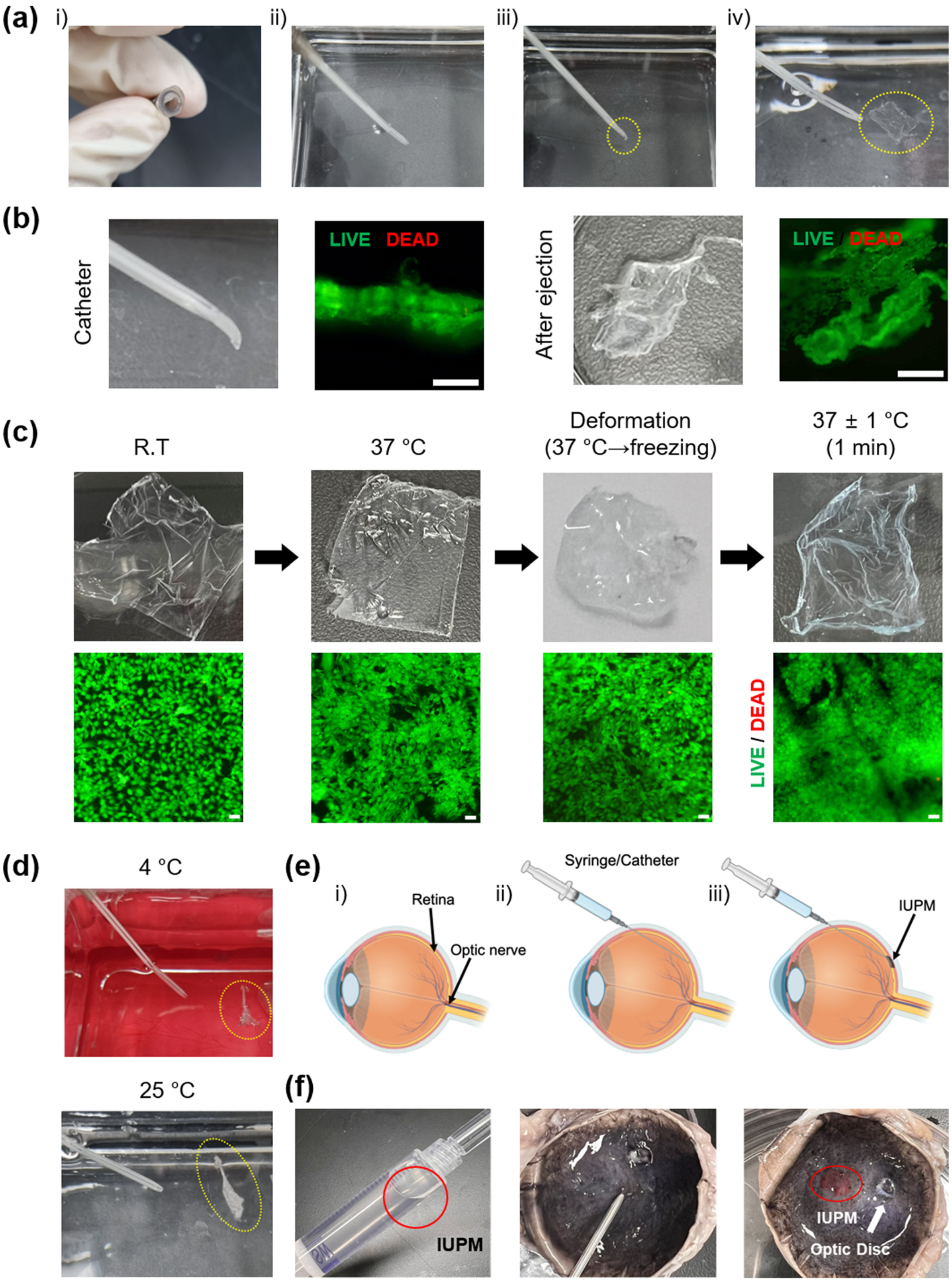

Fig. 5 Catheter-injectability and shape-memory effect of IUPM. (a) The IUPM demonstrates injectability and self-expandability when immersed in a 37 °C water bath. (i) Placement of the fixed IUMP, after deformation and freezing, at the catheter hub. (ii) Preparation for injectability evaluation by immersing the catheter in water at 37 °C. (iii) Image of the IUPM passing through the catheter. (iv) The IUPM recovering its original shape in 37 °C water. (b) Images illustrating the catheter-injectability of the IUPM. Fluorescence microscopy images showing live/dead staining of ARPE-19 cells 24 hours after seeding on IUPMs. Live cells are stained green, and dead cells are stained red (scale bar = 50 μm). (c) Images illustrating the shape-memory effect of the IUPMs (upper row). Fluorescence microscopy images showing live/dead staining of ARPE-19 cells 24 hours after seeding on IUPMs (lower row). Live cells are stained green, and dead cells are stained red (scale bar = 50 μm). (d) The IUPM shows no shape-memory effect at 4 °C (upper) and room temperature (lower). (e) *Ex vivo* injection of an IUPM into the subretinal space of a bovine eye: (i) fresh bovine eye, (ii) subretinal injection of PBS to create a space for the IUPM, and (iii) injection of the IUPM using a 16 G intravenous catheter. The figure was created using **https://BioRender.com**. (f) Images of the injected and expanded IUPM stained with rhodamine B.

shape-memory effect of the IUPM provides an optimal environment for the stable adhesion of the ARPE monolayer to the complex retinal surface, supporting the viability of transplanted cells.

Experimental section

Materials

Poly(L-lactide-*co*-caprolactone) (PLCL) with a composition ratio of L-lactide : ε-caprolactone of 50 : 50 and a molecular weight of 102 kDa was synthesized according to a previously reported method.[52] Poly(D,L-lactide-*co*-glycolide) (PLGA) with a composition ratio of lactide to glycolide of 75 : 25 and a molecular weight range of 66–107 kDa was purchased from Sigma-Aldrich (USA). Chloroform was obtained from DAEJUNG (Siheung, South Korea). Additionally, materials prepared for this study included a catheter (BD Angiocath Plus, NJ, USA), a silicon wafer with a diameter of 100 mm and a thickness of 525 μm, a 12-well Transwell plate with a 0.4 μm pore size (Corning, NY, USA), and an intravenous (I.V.) catheter (16 G, REF 382457; BD Angiocath Plus, NJ, USA).

Preparation of injectable ultrathin porous membranes (IUPMs)

Injectable ultrathin porous membranes (IUPMs) were prepared by blending two different polymers, PLGA and PLCL, in various blend ratios: PLCL1/PLGA2, PLCL1/PLGA1, and PLCL2/PLGA1, corresponding to weight ratios of 1 : 2, 1 : 1, and 2 : 1, respectively, following a previously reported procedure.[26] The polymers were dissolved in chloroform at a concentration of 5 w/v% to prepare IUPMs using the vapor-induced phase separation (VIPS) technique.[30] The solution was cast onto a Si substrate, and various relative humidity (RH) conditions were applied as 40%, 60%, and 80% using a spin-coating process for a porous surface structure and nanothin thickness. The spinning rate was 1000 rpm for 10 s followed by 2000 rpm for 10 s until the solvent was fully evaporated. Then, the freestanding IUPM was obtained by peeling off the membrane from the Si substrate in an aqueous environment.

Surface morphology characterization of IUPMs

The IUPMs with various blend ratios at different RHs were analyzed for surface pore morphologies using a scanning electron microscope (SEM, Phenom Pro, Thermo Scientific, MA, USA) and an atomic force microscope (AFM, XE 100, Park Systems, South Korea). The sample used for AFM measurements was prepared with dimensions of 1 × 1 cm. The measurements were conducted using the non-contact mode configuration for the AFM probe (PPP-NCHR 10M, Park Systems, South Korea) to ensure detailed surface characterization. The average pore size and porosity of the IUPMs were determined using ImageJ software (the National Institute of Mental Health, USA). AFM images were converted to a black-and-white binary phase, where the proportion of the black area relative to the total area was used to calculate the membrane's porosity. The water contact angle of IUPMs was evaluated using a contact angle analyzer (SmartDrop, Seongnam, South Korea), with a droplet volume of 10 μl.

Physical property characterization of IUPMs

The thickness of IUPMs was measured using a stylus profiler (Alpha-Step IQ, KLA, CA, USA) with a scan length of 2000 μm and a scan speed of 50 μm s^{-1}. The tensile properties for each blend ratio were assessed using a universal testing machine (UTM, Series 5960, Instron, MA, USA). Non-porous films with a thickness of 0.18 mm were utilized as the samples for the measurement. Each sample, 20 mm × 35 mm in size, was measured with an extension rate of 5 mm min^{-1} and a tensile strain (extension) with a gauge length of 100 mm. The modulus of resilience and Young's modulus were derived from the stress–strain curves.

Shape-memory property characterization of IUPMs

The shape-memory behavior of non-porous films (PLCL1/PLGA1) with a strip geometry (27 mm × 5 mm × 0.38 mm) was evaluated. The samples were immersed in a 37 °C water bath for 20 minutes to induce thermal activation, followed by deformation. The deformed films were stored in a freezer for 20 minutes. After freezing, the films were placed back in the 37 °C water bath to observe the shape recovery behavior. Furthermore, the shape-memory effect was measured by dynamic mechanical analysis (DMA, MCR 702e, Anton Paar, Austria) in tensile mode, following a previously described process.[26] Rectangular non-porous film samples (20 mm × 35 mm × 0.6 mm) were cut from films prepared by the solvent casting method. In this process, vacuum drying was applied instead of spin-coating to obtain a film with a thickness suitable for the jig. The rectangular sample was initially loaded under 0 N and then heated to 55 °C for 10 minutes under extensional stress, applied at a rate of 0.05 MPa min^{-1}, until reaching 0.15 MPa. This step allowed the polymer to memorize the shape. The sample was then cooled to −4 °C at a rate of 5 °C min^{-1}, maintaining this temperature for 3 minutes to fix the polymer chains in the temporary shape while gradually decreasing the extensional stress to 0 MPa. During this cooling step, the kinetic energy of the polymer was converted to potential energy. Finally, the sample was reheated to 55 °C at a rate of 5 °C min^{-1}, releasing the stored energy, which caused the polymer chains to move, resulting in an observable change in extensional strain.

The shape-recovery ratio (R_r) and shape-fixity ratio (R_f) of the IUPM were calculated using the following equations:

$$R_r\ (\%) = \frac{\varepsilon_{\text{defom}} - \varepsilon_{\text{final}}}{\varepsilon_{\text{defom}} - \varepsilon_{\text{begin}}} \times 100 \tag{1}$$

$$R_f\ (\%) = \frac{\varepsilon_{\text{un}}}{\varepsilon_{\text{max}}} \times 100 \tag{2}$$

where $\varepsilon_{\text{begin}}$, $\varepsilon_{\text{deform}}$, and $\varepsilon_{\text{final}}$ represent the extensional strain value at the beginning, and in the deformed and recovered states, respectively. ε_{un} denotes the strain after unloading, and ε_{un} indicates the maximum extensional strain.

Thermal property assessment *via* differential scanning calorimetry (DSC)

Approximately 30 mg of porous membranes, prepared at various blending ratios, were loaded into sealed aluminum pans.

Table 1 qRT-PCR primer sequences

Gene	Forward (5′–3′)	Reverse (5′–3′)
GAPDH	GTCTCCTCTGACTTCAACAGCG	ACCACCCTGTTGCTGTAGCCAA
ZO-1	AGCCTGCAAAGCCAGCTCA	AGTGGCCTGGATGGGTTCATAG
CLAUDIN	GCATGAAGTGTATGAAGTGCTTGGA	CGATTCTATTGCCATACCATGCTG
RPE65	TTTGGCACCTGTGCTTTCCCAG	GTTGGTCTCTGTGCAAGCGTAG
CRALBP	CCTACAATGTGGTCAAGCCCTTC	CGAAGTCAGAGGGCAGGATGTT

All measurements were conducted under nitrogen purge at a flow rate of 50 mL min^{-1}. Each sample was placed in an Al pan and applied to the cell of the DSC unit (DSC Q10, TA Instruments, DE, USA). The temperature range was set from −60 °C to 200 °C, with both heating and cooling rates at 10 °C min^{-1}.

Cell viability assessment

ARPE-19 cells (ATCC, Manassa, VA, USA) were cultured at 37 °C with 5% CO_2 in Dulbecco's modified Eagle's medium/nutrient mixture F-12 (DMEM/F-12; Gibco BRL, Gaithersburg, MD, USA) supplemented with 10% (v/v) fetal bovine serum (Gibco BRL) and 1% (v/v) penicillin–streptomycin (Gibco BRL). Cell viability was evaluated using the neutral red (NR) assay and the terminal deoxynucleotide transferase-mediated deoxyuridine triphosphate nick end labeling (TUNEL) staining. ARPE-19 cells were seeded in wells or on IUPMs at a density of 10^4 cells per cm^2 and incubated for 24 hours. After incubation, the cells were washed with phosphate buffered saline (PBS; Gibco BRL) and then incubated with NR solution (0.005% (w/v), Sigma Aldrich) for an additional 2–3 hours at 37 °C. Following incubation, the cells were washed with PBS, and an elution medium (50% EtOH and 1% acetic acid) was added. The plates were gently shaken for 10 minutes. The optical density (OD) of each well was recorded at 540 nm using a microplate reader (GloMax Discover, Promega, USA). TUNEL staining was performed using an ApopTag® fluorescein *in situ* apoptosis detection kit (Millipore, Billerica, MA, USA) according to the manufacturer's protocol. The cells were counterstained with 4,6-diamidino-2-phenylindole (DAPI; Vector Laboratories, Burlingame, CA, USA) and examined under a fluorescence microscope (ECLIPSE Ts2R, Nikon, Tokyo, Japan).

F-actin and ZO-1 staining

ARPE-19 cells were seeded in wells or IUPMs at a density of 5 × 10^4 cells per cm^2 and incubated for 24 hours. After incubation, the cells were washed with PBS (Gibco BRL) and then fixed with 4% paraformaldehyde (Biosesang, Sungnam, Korea) for 10 minutes at room temperature. For immunocytochemistry, the samples were stained with FITC-conjugated anti-ZO-1 (Thermo Fisher, MA, USA). For F-actin staining, the samples were stained with TRITC-phalloidin containing a mounting medium (VECTASHIELD H-1600, Vector, Burlingame, CA, USA), counterstained with 4′,6-diamidino-2-phenylindole (DAPI, Vector), and then examined using a fluorescence microscope (ECLIPSE Ts2R, Nikon, Tokyo, Japan).

Quantitative real-time PCR (qRT-PCR)

Total RNA was extracted from the samples using 1 mL of QIAzol (Qiagen, Germantown, MD, USA) and 200 μL of chloroform (Sigma-Aldrich, USA). The samples were centrifuged at 12 000 rpm for 10 min at 4 °C. The RNA pellet was washed with 75% (v/v) ethanol (Sigma-Aldrich, USA) in water and dried. After drying, the samples were dissolved in RNase-free water (Invitrogen Co., CA, USA). Reverse transcription was performed using 1.5 μg of pure total RNA and primescript RT master mix (TaKaRa, Kusatsu, Japan), followed by PCR amplification of the synthesized cDNA. For qRT-PCR, TB Green® Premix Ex Taq™ (Tli RNase H Plus) (TaKaRa) and a real-time PCR detection system (Thermo Fisher) were used. GAPDH served as the internal control. The sequences of primers used for qRT-PCR are listed in Table 1.

In vitro injection test

IUPMs were prepared as 1 cm × 1 cm squares and deformed at 37 °C. The deformed IUPMs were then frozen by storing them in a freezer (−22 °C) for 20 minutes. After freezing, the IUPMs were placed in a catheter hub and injected into water at temperatures of 4 °C, 25 °C, and 37 °C using a syringe. The viability of the IUPMs was assessed using a LIVE/DEAD® viability/cytotoxicity kit (Invitrogen Co.). For cell culture, IUPMs were fixed to Transwell hanging cell culture inserts. After 24 hours of cell culture, the ARPE-19/IUPM constructs were gently rinsed with PBS and carefully released from the Transwell insert. The APRE-19/IUPM constructs were then subjected to the stages of room temperature (RT), deformation, and recovery. In the final step, IUPMs were injected through a 16 G catheter. Subsequently, the samples at all stages were stained with a LIVE/DEAD® viability/cytotoxicity kit at 37 °C for 10 minutes. Finally, the samples were imaged using a fluorescence microscope (ECLIPSE Ts2R, Nikon, Tokyo, Japan).

Ex vivo injection test

Refrigerated bovine eyes were obtained from a local slaughterhouse and transported to the laboratory while maintaining a cold chain to ensure tissue integrity. The eyes were washed with phosphate-buffered saline (PBS). A rhodamine B stained IUPM was loaded into a 16-gauge needle attached to a syringe filled with PBS. A small incision was made in the sclera of the bovine eyes. The needle was carefully inserted through the incision, and the IUPM was injected into the subretinal space. After the injection, the needle was carefully withdrawn from the eye.

Conclusions

In this study, we successfully fabricated injectable ultrathin porous membranes (IUPMs) using a polymer blend of PLCL and PLGA. The blend ratios were optimized to enhance shape-memory properties, with the PLCL1/PLGA1 ratio emerging as the most suitable due to its exceptional shape recovery at 37 °C. The resulting membranes were thoroughly characterized for their porous structure, mechanical properties, and biocompatibility. Under varying relative humidity conditions, the membranes exhibited optimal pore size and thickness, while their hydrophilic surfaces supported cell adhesion and growth, as evidenced by the NR assay and TUNEL staining, which indicated minimal cytotoxicity and high cell viability. Further assessments revealed that the RH 60% IUPM group promoted enhanced epithelial barrier formation, as demonstrated by increased F-actin and ZO-1 expression, indicating robust cytoskeletal organization and tight junction integrity. Additionally, key genes such as CLAUDIN and CRALBP were more highly expressed in this group, highlighting the membranes' potential for retinal regeneration applications. The catheter-injectability and self-expandability of IUPMs were validated through successful ejection and expansion at 37 °C, maintaining high cell viability throughout the process. *Ex vivo* experiments confirmed the practicality of delivering IUPMs into the subretinal space of a bovine eye, demonstrating their potential as scaffolds for tissue-engineered retinal RPE transplantation. Overall, the outcomes of this study suggest that IUPMs, particularly those with a PLCL1/PLGA1 blend ratio, are promising candidates for biomedical applications, especially in retinal tissue engineering. Their biocompatibility, shape-memory properties, and ability to support cell growth and function underscore their potential for therapeutic use in regenerative applications. Based on these results, future studies will focus on optimizing the RH conditions to precisely control the pore size and porosity while investigating and examining their correlation relationship with shape recovery. Additionally, co-culture experiments aimed at developing multilayered structures—facilitating integration with multilayered neural retina—may prove valuable for constructing 3D retinal tissue regeneration scaffolds. Furthermore, *in vivo* evaluations will be performed to validate the *in vitro* findings and assess the membranes' therapeutic potential in clinical settings.

Author contributions

SeongHoon Jo: writing – original draft, visualization, validation, methodology, investigation, data curation, and conceptualization. Yu-Jin Kim: writing – original draft, visualization, validation, methodology, investigation, and data curation. Taek Hwang: investigation. Se Youn Jang: investigation. So-Jin Park: investigation. Seongryeol Ye: investigation. Youngmee Jung: writing – review & editing and supervision. Jin Yoo: writing – review & editing, supervision, funding acquisition, and conceptualization.

Data availability

The data supporting this article have been included as part of the ESI.†

Conflicts of interest

The authors declare no conflicts of interest.

Acknowledgements

This work was financially supported by the National R&D Program through the National Research Foundation of Korea (NRF) grant funded by the Ministry of Science and ICT (RS-2023-00211412, RS-2024-00440151) and the KIST research program (2E33151). TOC created with **https://Biorender.com**.

Notes and references

1 H. Vyawahare and P. Shinde, *Cureus*, 2022, **14**, e29583.
2 J. T. Lu, C. J. Lee, S. F. Bent, H. A. Fishman and E. E. Sabelman, *Biomaterials*, 2007, **28**, 1486–1494.
3 T. Xia and L. J. Rizzolo, *Vision Res.*, 2017, **139**, 72–81.
4 C. Scimone, L. Donato, S. Alibrandi, M. Vadala, G. Giglia, A. Sidoti and R. D'Angelo, *Exp. Eye Res.*, 2021, **209**, 108641.
5 Y. Lu, M. Lin, J. Zong, L. Zong, Z. Zhao, S. Wang, Z. Zhang and M. Han, *Food Sci. Nutr.*, 2020, **8**, 6415–6425.
6 E. Borrelli, D. Sarraf, K. B. Freund and S. R. Sadda, *Prog. Retinal Eye Res.*, 2018, **67**, 30–55.
7 H. Khalili, H. H. Kashkoli, D. E. Weyland, S. Pirkalkhoran and W. R. Grabowska, *Pharmaceuticals*, 2023, **16**, 620.
8 N. Jemni-Damer, A. Guedan-Duran, M. Fuentes-Andion, N. Serrano-Bengoechea, N. Alfageme-Lopez, F. Armada-Maresca, G. V. Guinea, J. Perez-Rigueiro, F. Rojo, D. Gonzalez-Nieto, D. L. Kaplan and F. Panetsos, *Front. Bioeng. Biotechnol.*, 2020, **8**, 588014.
9 M. Luo and Y. Chen, *Int. J. Ophthalmol.*, 2018, **11**, 150–159.
10 S. Rahmani, F. Tabandeh, S. Faghihi, G. Amoabediny, M. Shakibaie, B. Noorani and F. Yazdian, *Int. J. Polym. Mater. Polym. Biomater.*, 2017, **67**, 27–35.
11 D. S. R. Nair, M. J. Seiler, K. H. Patel, V. Thomas, J. C. M. Camarillo, M. S. Humayun and B. B. Thomas, *Appl. Sci.*, 2021, **11**, 2154.
12 S. S. Rohiwal, Z. Ellederova, T. Ardan and J. Klima, *Biomedicines*, 2021, **9**, 1005.
13 A. Maddalena, P. Tornabene, P. Tiberi, R. Minopoli, A. Manfredi, M. Mutarelli, S. Rossi, F. Simonelli, J. K. Naggert, D. Cacchiarelli and A. Auricchio, *Mol. Ther.*, 2018, **26**, 524–541.
14 Y. Haraguchi, T. Shimizu, M. Yamato and T. Okano, *RSC Adv.*, 2012, **2**, 2184–2190.
15 K. Ben M'Barek, S. Bertin, E. Brazhnikova, C. Jaillard, W. Habeler, A. Plancheron, C. M. Fovet, J. Demilly, M. Jarraya, A. Bejanariu, J. A. Sahel, M. Peschanski, O. Goureau and C. Monville, *Biomaterials*, 2020, **230**, 119603.
16 H. Liu, S. S. Huang, G. Lingam, D. Kai, X. Su and Z. Liu, *Stem Cell Res. Ther.*, 2024, **15**, 390.
17 V. Klymenko, O. G. Gonzalez Martinez and M. Zarbin, *Stem Cells Transl. Med.*, 2024, **13**, 317–331.
18 M. Abedin Zadeh, M. Khoder, A. A. Al-Kinani, H. M. Younes and R. G. Alany, *Drug Discovery Today*, 2019, **24**, 1669–1678.

19 S. Hammadi, N. Tzoumas, M. Ferrara, I. P. Meschede, K. Lo, C. Harris, M. Lako and D. H. Steel, *J. Clin. Med.*, 2023, **12**, 2870.

20 A. Lakkaraju, A. Umapathy, L. X. Tan, L. Daniele, N. J. Philp, K. Boesze-Battaglia and D. S. Williams, *Prog. Retinal Eye Res.*, 2020, 100846, DOI: **10.1016/j.preteyeres.2020.100846**.

21 M. P. Nikolova and M. S. Chavali, *Bioact. Mater.*, 2019, **4**, 271–292.

22 L. Suamte, A. Tirkey, J. Barman and P. Jayasekhar Babu, *Smart Mater. Manuf.*, 2023, **1**, 100011.

23 P. Zarrintaj, F. Seidi, M. Youssefi Azarfam, M. Khodadadi Yazdi, A. Erfani, M. Barani, N. P. S. Chauhan, N. Rabiee, T. Kuang, J. Kucinska-Lipka, M. R. Saeb and M. Mozafari, *Composites, Part B*, 2023, **258**, 110701.

24 H. K. Makadia and S. J. Siegel, *Polymers*, 2011, **3**, 1377–1397.

25 D. C. Surrao, U. Greferath, Y. Q. Chau, S. J. Skabo, M. Huynh, K. J. Shelat, I. J. Limnios, E. L. Fletcher and Q. Liu, *Acta Biomater.*, 2017, **64**, 357–376.

26 K. J. Cha, E. Lih, J. Choi, Y. K. Joung, D. J. Ahn and D. K. Han, *Macromol. Biosci.*, 2014, **14**, 667–678.

27 J. Yoo, T. H. Kim, S. Park, K. Char, S. H. Kim, J. J. Chung and Y. Jung, *Adv. Funct. Mater.*, 2021, **31**, 2008172.

28 J. Lee, J. Yoo, J. Kim, Y. Jang, K. Shin, E. Ha, S. Ryu, B. G. Kim, S. Wooh and K. Char, *ACS Appl. Mater. Interfaces*, 2019, **11**, 6550–6560.

29 S. Ryu, J. Yoo, Y. Jang, J. Han, S. J. Yu, J. Park, S. Y. Jung, K. H. Ahn, S. G. Im, K. Char and B. S. Kim, *ACS Nano*, 2015, **9**, 10186–10202.

30 S. Ryu, J. Yoo, J. Han, S. Kang, Y. Jang, H. J. Han, K. Char and B.-S. Kim, *Chem. Mater.*, 2017, **29**, 5134–5147.

31 J. Yoo, Y. Jung, K. Char and Y. Jang, *Trends Biotechnol.*, 2023, **41**, 214–227.

32 L. Lu, C. A. Garcia and A. G. Mikos, *J. Biomater. Sci., Polym. Ed.*, 1998, **9**, 1187–1205.

33 R. Duan, Y. Wang, Y. Zhang, Z. Wang, F. Du, B. Du, D. Su, L. Liu, X. Li and Q. Zhang, *ACS Omega*, 2021, **6**, 18300–18313.

34 Y. Hua, Y. Su, H. Zhang, N. Liu, Z. Wang, X. Gao, J. Gao and A. Zheng, *Drug Delivery*, 2021, **28**, 1342–1355.

35 S. Ryu, C. Lee, J. Park, J. S. Lee, S. Kang, Y. D. Seo, J. Jang and B. S. Kim, *Angew. Chem., Int. Ed.*, 2014, **53**, 9213–9217.

36 P. Gentile, V. Chiono, I. Carmagnola and P. V. Hatton, *Int. J. Mol. Sci.*, 2014, **15**, 3640–3659.

37 Y. C. Sun, M. Chu, M. Huang, O. Hegazi and H. E. Naguib, *Macromol. Mater. Eng.*, 2019, **304**, 1900196.

38 M. Pantoja, P.-Z. Jian, M. Cakmak and K. A. Cavicchi, *ACS Appl. Polym. Mater.*, 2019, **1**, 414–424.

39 J. Peng, Y. Han, Y. Yang and B. Li, *Polymer*, 2004, **45**, 447–452.

40 M. Behl and A. Lendlein, *Mater. Today*, 2007, **10**, 20–28.

41 P. Feng, R. Y. Zhao, F. Yang, S. P. Peng, H. Pan and C. J. Shuai, *Virtual Phys. Prototyping*, 2024, **19**, e2290186.

42 T. Yue, J. He, L. Tao and Y. Li, *J. Chem. Theory Comput.*, 2023, **19**, 4641–4653.

43 W. Yan, Y. Ding, R. Zhang, X. Luo, P. Sheng, P. Xue and J. He, *Polymer*, 2022, **239**, 124436.

44 D. G. Barrett and M. N. Yousaf, *Molecules*, 2009, **14**, 4022–4050.

45 S. F. Chou and K. A. Woodrow, *J. Mech. Behav. Biomed. Mater.*, 2017, **65**, 724–733.

46 S. Ryu, J. Yoo, J. Han, S. Kang, Y. Jang, H. J. Han, K. Char and B. S. Kim, *Chem. Mater.*, 2017, **29**, 5134–5147.

47 Y. Jang, H. Lee, K. Char and J. M. Nam, *Adv. Mater.*, 2015, **27**, 1893–1899.

48 M. Namhongsa, D. Daranarong, R. Molloy, S. Ross, G. M. Ross, A. Tuantranont, D. Boonyawan, J. Tocharus, S. Sivasinprasasn, P. D. Topham, B. J. Tighe and W. Punyodom, *Eur. Polym. J.*, 2023, **194**, 112135.

49 E. Y. S. Tan, S. Agarwala, Y. L. Yap, C. S. H. Tan, A. Laude and W. Y. Yeong, *J. Mater. Chem. B*, 2017, **5**, 5616–5622.

50 J. Kim, J. Y. Park, J. S. Kong, H. Lee, J. Y. Won and D. W. Cho, *Int. J. Mol. Sci.*, 2021, **22**, 1095.

51 T. Fujie, Y. Mori, S. Ito, M. Nishizawa, H. Bae, N. Nagai, H. Onami, T. Abe, A. Khademhosseini and H. Kaji, *Adv. Mater.*, 2014, **26**, 1699–1705.

52 S. I. Jeong, B. S. Kim, S. W. Kang, J. H. Kwon, Y. M. Lee, S. H. Kim and Y. H. Kim, *Biomaterials*, 2004, **25**, 5939–5946.